REPORT DOCUMENTATION PAGE

Form Approved
OMB No. 074-0188

1. AGENCY USE ONLY (Leave blank)	2. REPORT DATE	3. REPORT TYPE AND DATES COVERED
	1998	Proceedings

4. TITLE AND SUBTITLE
Experimental and CFD Studies of Non-Thermal Plasmas for NOx Control

5. FUNDING NUMBERS
N/A

6. AUTHOR(S)
M.J. Nusca, P.A. Sagear, and A.W. Miziolek

7. PERFORMING ORGANIZATION NAME(S) AND ADDRESS(ES)
U.S. Army Research Laboratory, AMSRL-
WM-PC, Aberdeen Proving Ground, MD
24005-5066

8. PERFORMING ORGANIZATION REPORT NUMBER
N/A

9. SPONSORING / MONITORING AGENCY NAME(S) AND ADDRESS(ES)
SERDP
901 North Stuart St. Suite 303
Arlington, VA 22203

10. SPONSORING / MONITORING AGENCY REPORT NUMBER
N/A

11. SUPPLEMENTARY NOTES

12a. DISTRIBUTION / AVAILABILITY STATEMENT
Approved for public release: distribution is unlimited.

12b. DISTRIBUTION CODE
A

13. ABSTRACT ***(Maximum 200 Words)***

Non-thermal plasmas (NTPs) represent a promising technology for the destruction of various toxic gases entrained in air streams. One challenging example of the need for hazardous gas control is the jet engine test cell (JETC) facility where very large amounts of NO_xs are emitted along with various hydrocarbon gases on an episodic basis. The high flow rates as well as the wide dynamic range of pollutant concentrations make this a particularly difficult problem for emissions control.

In order to investigate the ability of NTPs to dissociate NO_xs, will be entrained in an airstream and passed through the reactor. We will measure the concentrations of various radicals produced in the reactor by the destruction of NO_x. This data will be compared to results generated using a computational model of the reactor.

19991202 047

14. SUBJECT TERMS
SERDP, CFD, Non-thermal plasma, NOx, jet engine test cell.

15. NUMBER OF PAGES
5

16. PRICE CODE
N/A

17. SECURITY CLASSIFICATION OF REPORT	18. SECURITY CLASSIFICATION OF THIS PAGE	19. SECURITY CLASSIFICATION OF ABSTRACT	20. LIMITATION OF ABSTRACT
unclass	unclass	unclass	UL

NSN 7540-01-280-5500

Standard Form 298 (Rev. 2-89)
Prescribed by ANSI Std. Z39-18
298-102

Experimental and CFD Studies of Non-Thermal Plasmas for NO_x Control

M.J. Nusca, P.A. Sagear*, A.W. Miziolek

U.S. Army Research Laboratory, AMSRL-WM-PC
Aberdeen Proving Ground, MD 21005-5066 USA

We present some early results of a comprehensive experimental and modeling study to understand the driving physical and chemical processes involved in non-thermal plasma control of toxic gases such as the NO_xs.

1. Introduction

Non-thermal plasmas (NTPs) represent a promising technology for the destruction of various toxic gases entrained in air streams. One challenging example of the need for hazardous gas control is the jet engine test cell (JETC) facility where very large amounts of NO_xs are emitted along with various hydrocarbon gases on an episodic basis. The high flow rates as well as the wide dynamic range of pollutant concentrations make this a particularly difficult problem for emissions control.

In order to investigate the ability of NTPs to dissociate NO_xs, we have constructed a small scale channel-flow reactor with wall-mounted plasma discharge sites. Toxic gaseous mixtures, including NO_xs, will be entrained in an airstream and passed through the reactor. We will measure the concentrations of various radicals produced in the reactor by the destruction of NO_x. This data will be compared to results generated using a computational model of the reactor. Our approach consists of closely coupled experimental and computational efforts to better understand the detailed chemistry and physics as well as to simulate and scale-up plasma reactors.

2. Experimental

The laser induced fluorescence (LIF) experiment is similar to that used by other investigators [1,2] so only a brief outline of the instrument is given here. The laser system for both LIF and planar LIF (PLIF) experiments for OH detection consists of a Lambda Physik Compex 102 XeCl excimer laser, a Scanmate 2 dye laser using Coumarin 540 dye, and a second harmonic generator.

For single-point LIF measurements, the laser system is tuned to the (1-0) band of the $A^2\Sigma$-$X^2\Pi$ system around 283 nm and focused into the plasma reactor. The red-shifted fluorescence is centered near 315 nm (Fig. 1) and is collected with a two-lens condenser system (Fig. 2). The fluorescence is passed through a broad-band interference filter centered at 310nm (50 nm bandwidth) before detection by a PMT (Phillips XP2018B or Hamamatsu R928). After passing through a preamplifier, the signal is averaged with

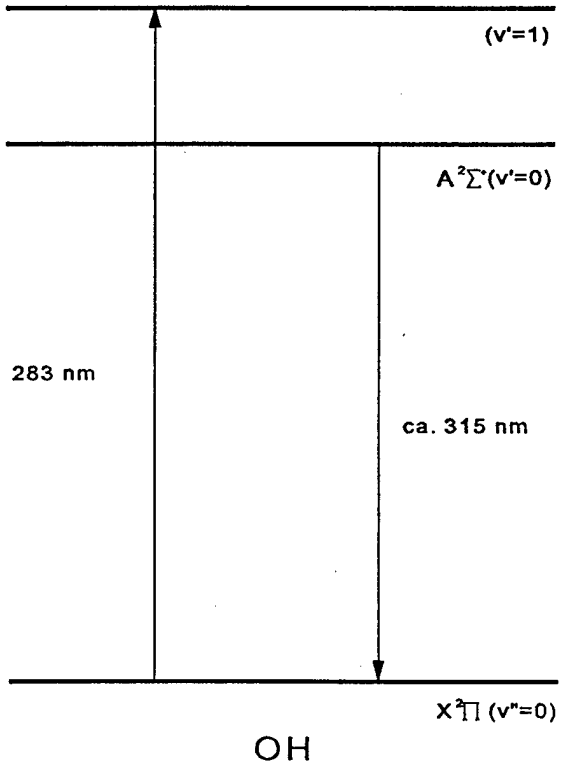

Figure 1. Energy Level Diagram for OH radical.

a SRS SR250 boxcar integrator and stored in a PC. The laser intensity is measured with a Scientech AC25HD calorimeter connected to an A/D converter and stored in the PC. Dispersed fluorescence spectra are measured by focusing the

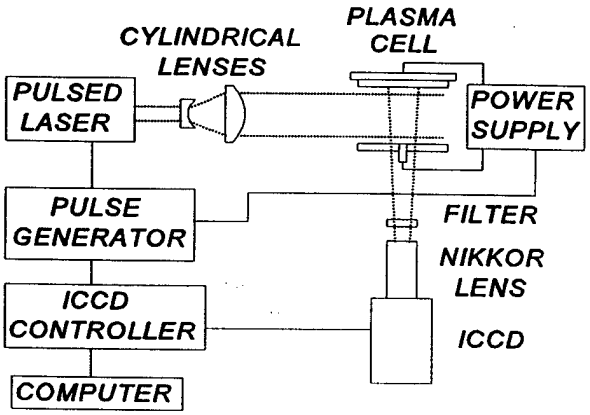

Figure 2. Schematic Diagram for PLIF studies.

fluorescence into an Acton Research Corporation S300i monochromator and detecting the dispersed light with either the Hamamatsu PMT or a Princeton Instruments IRY-1024G intensified photodiode array.

PLIF measurements of OH are made by forming a laser sheet with two cylindrical lenses, one negative and one positive focal length (Fig. 2). The sheet is passed through the plasma reactor and, after passing through an interference filter, the red-shifted fluorescence is detected with an intensified CCD detector (Princeton Instruments ITE/CCD-576G/RB-E) equipped with a UV Nikkor camera lens. The transverse intensity of the laser sheet is simultaneously monitored by using a fused silica microscope slide to direct a fraction of the laser sheet to a cell containing a highly concentrated R6G dye solution. Another camera (Cohu 4710) detects an image of the resulting fluorescence. The images are stored in a PC for off-line image processing later.

The plasma cells use both a point-plane corona discharge and a silent discharge geometry and were constructed at LANL. The power supply provides high voltage pulses up to 50 kV in amplitude and about 25 ns in duration. Current and voltage profiles are simultaneously measured to monitor the energy density supplied to the reactor.

In addition to the detection measurements on OH radicals as discussed above, temperature measurements on the plasma can be made through analysis of the relative intensities of fluorescent bands obtained by scanning the frequency of the dye laser which has a bandwidth of 0.15 cm^{-1}. An important step in this process involves the determination of the ground-state energy levels from the relative fluorescence intensities of transitions involving known rovibronic levels. The population of a vibrational level in the ground electronic state is simply related to the signal intensity by the expression

$$I_f = K \Phi_f B_{if} N_i I_l \qquad (1)$$

where I_f is the signal intensity and I_l is that of the laser. B_{if} is the stimulated absorption coefficient for the transition, and Φ_f is the fluorescence yield which can be calculated from stimulated emission coefficients and nonradiative decay rates due to quenching and predissociation [3,4]. The Einstein coefficients and ground-state rotational energies are all readily available [5-8].

The relative populations are matched with the ground-state energies and the data points are plotted and fit to a straight line according to Eq. (2).

$$N_i = g_i e^{-\frac{E_i}{kT}} \qquad (2)$$

The transitions of interest for temperature measurements are in the (0,0) band of the $A^2\Sigma$ - $X^2\Pi$ system around 307 nm. [3]. This approach is based upon the assumption of rotational equilibrium of OH in the non thermal plasma; we are continuing to investigate the validity of this hypothesis.

Our measurements include the detection of other radicals. In particular O, H, and N atoms can be detected in the plasma. The detection schemes for these atoms invariably involve the use of two-photon spectroscopy due to the difficulty of generating vacuum UV radiation. The energy level diagrams for these species are shown in Fig. 3 and are based on previously reported work [9-13].

Data from the experimental reactor is forthcoming and will be reported in future papers. One of the goals of the present study is the comparison of these data with a computational fluid dynamics (CFD) model. This model is described in the next section and the comparison between data and the model will be reported in future papers.

3. CFD

A computational fluid dynamics code, used to simulate multi-component, gaseous, chemically reacting flows in various gasdynamic applications, has been modified for numerical simulation of the plasma reactor system. The ARL-NSRG2 code was written at the Army Research Laboratory for solution of the 2D/axisymmetric Navier-Stokes equations including species diffusion, thermal conduction, viscosity, and nonequilibrium chemical kinetics [14]. An explicit fourth-order Runge-Kutta algorithm is utilized for time-integration. The convective and transport terms are resolved using central-differencing. Numerical stiffness due to chemical source terms is mitigated by convergence acceleration techniques. Flow turbulence, introduced as an in-flow condition, is modeled using a mixing length approach.

The electrons added by the plasma through microdischarges in the flow field are modeled using source terms in the species mass conservation equations. These discharges promote chemical reactions in regions of the flow field interacting with the plasma. An initial NO_x chemical kinetics mechanism, incorporated into the code, includes 9 reactions and 12 species. The reactions considered consist of three dissociation reactions (O_2, N_2, and H_2O to O,N, and OH), three ozone-producing reactions, and three reactions that produce NO and HNO_3 from O,N,OH, and NO_2.

Figure 4 shows the specific configuration used in this initial study to test the CFD code. The inflow is uniform, laminar, and consists of wet air and NO_2. Although the reactor has sides (i.e., 10 cm apart), the present CFD simulation was run as 2D along the centerplane of the reactor, as shown in the lower part of Figure 4. Plasma discharge locations were placed 10 cm apart and were assumed to discharge at a frequency of 1 kHz. Both the inflow and discharge temperatures were 300K. The lower part of Figure 4 shows the computational mesh, 100 cells in the flow direction and 40 cells in the transverse direction. The mesh is clustered near the reactor walls (i.e., plates) in order to increase accuracy of the computed wall boundary layers. The mesh is uniform in the flow direction. The four dark lines are not physical, but are added to indicate the locations of the discharges.

Figure 5 shows a representative result of CFD simulation. The top part of the figure displays the fully-developed flow in the channel (reactor) as velocity vectors overlaid with grey-scale contours of non-dimensional velocity. Boundary layers develop on the reactor walls (i.e., small vectors) and the core velocity is about 0.9. The bottom view of the figure displays grey-scale contours of electron mass fraction at the instant the discharges occur; at four locations the mass fraction of electrons is unity (dark) while elsewhere the mass fraction is null (white).

Figure 6 shows grey-scale contours of NO_2 mass fraction (note the restricted scale of mass fraction) at near the instant the discharges occur. Depletion of NO_2 occurs at the discharge sites as NO_2 reacts with O, N, and OH (formed by O_2, N_2 and H_2O reactions with electrons) to form NO and HNO_3. The bottom view of the figure shows the distribution of HNO_3, as number density, along the center of the reactor (i.e., x=0 to 50 cm, y=.15 cm) at various times. The discharge is occurring every 0.001s. The slow buildup of HNO_3 is indicative of reactions occurring to breakdown NO_2 throughout the reactor.

The major assumptions used in the present CFD simulations are laminar flow, certain reduced kinetics mechanism and rates, and certain

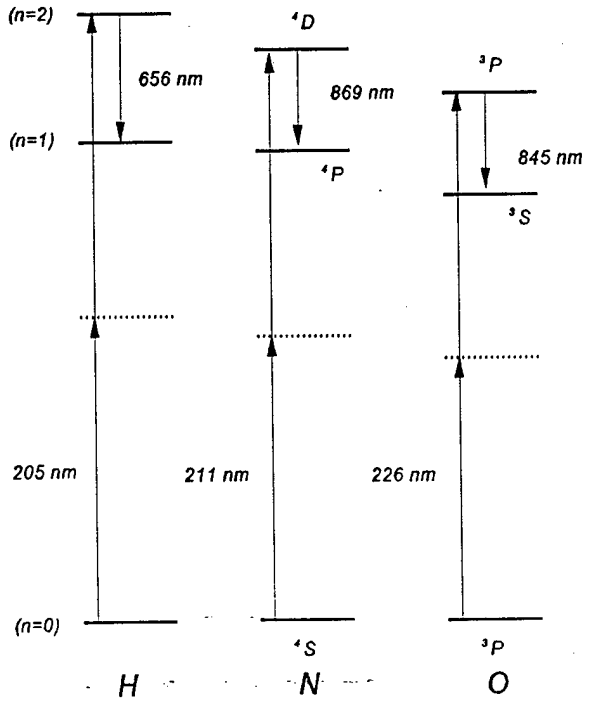

Figure 3. Energy level diagrams for H, N, and O atoms.

assumptions about diffusion and thermal properties of the species. The results shown in Figures 5 and 6 are influenced by these assumptions. The CFD code has been setup for the reactor problem and is now available to test the dependence of the results on the assumptions and do some further work. The introduction of turbulence in the inflow, at the walls and with flow obstructions will certainly effect these results.

Acknowledgement

Support has been provided by the tri-agency Strategic Environmental Research and Development Program (SERDP).

*NAS/NRC Postdoctoral Research Associate

References

[1] U. Meier, R. Kienle, I. Plath, and K. Kohse-Höinghaus, Ber. Bunsenges. Phys. Chem. **96** (1992) 1401.

[2] Ronald K. Hanson, Jerry M. Seitzman, and Phillip H. Paul, Appl. Phys. B. **50** (1990) 441.

[3] David R. Crosley and Jay B. Jeffries, Temperature Its Measurement and Control in Science and Industry, Vol. 6, ed. James F. Schooley (American Institute of Physics, New York, 1992) p. 701.

[4] William R. Anderson, Leon J. Decker, and Anthony J. Kotlar, Combustion and Flame 48 (1982) 163.

[5] G. H. Dieke, and E. M. Crosswhite, JQSRT 2 (1962) 97.

[6] A. Schadee. JQSRT 19 (1978) 451.

[7] I. L. Chidsey and D. R. Crosley JQSRT 23 (1980) 187.

[8] W. L. Dimpfl and J. L. Kinsey, JQSRT 21 (1979) 233.

[9] John E. M. Goldsmith, Applied Optics 29 (1990) 4841.

[10] B. E. Forch, J. B. Morris, and A. W. Miziolek, "Laser Induced Fluorescence and Ionization Techniques for Combustion Diagnostics", Book Chapter in Laser-Based Approaches in Luminescence Spectroscopy, T. Vo-Dinh and D. Eastwood, eds., ASTM Publication STP 1066, P. 50, Philadelphia, 1990.

[11] W. K. Bischel, B. E. Perry, David R. Crosley, Chem. Phys. Lett. 82 (1981) 85.

[12] A. W. Miziolek and M. A. DeWilde, Opt. Lett. 9 (1984) 390.

[13] P. J. Dagdigian, B. E. Forch, and A. W. Miziolek, Chem. Phys. Lett. 148 (1988) 299.

[14] M. J. Nusca, Proceedings of the 28th AIAA Plasmadynamics and Laser Conference, Atlanta, GA, June 23-25, 1997 (Paper No. 97-2359).

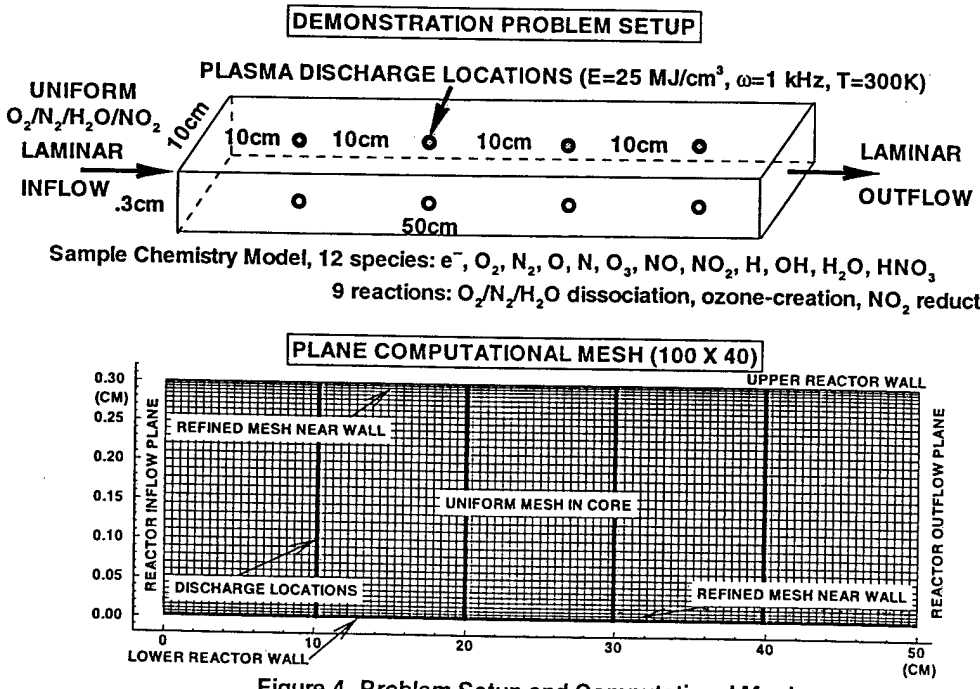

Figure 4. Problem Setup and Computational Mesh.

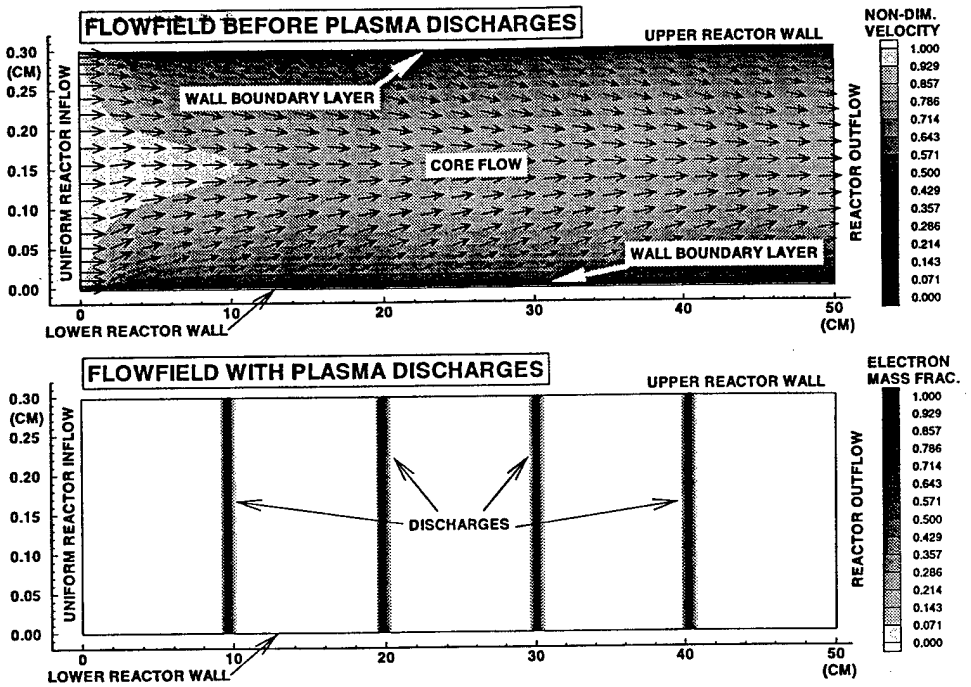

Figure 5. Computed Flowfields with and without Plasma Discharges.

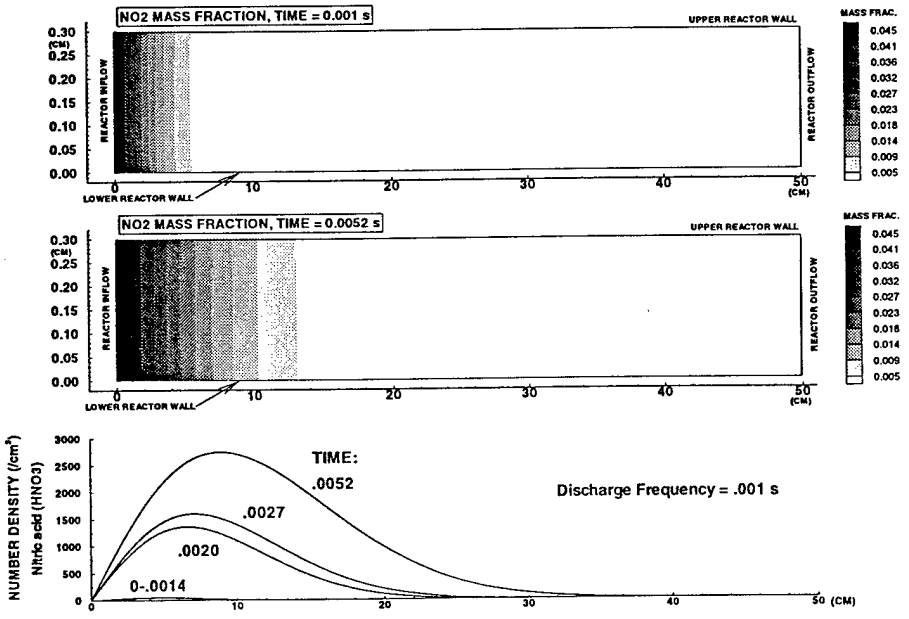

Figure 6. Computed NO_2 Flowfields and HNO_3 Distributions.